



Water Resources Research

RESEARCH ARTICLE

10.1002/2016WR020203

Key Points:

- We characterized the last centimeters of a bottom boundary layer using a bistatic high resolution acoustic profiler
- The device allows the direct determination of mixing coefficients and shear production at sub cm resolution
- The observations mainly agree well with constant stress layer theory while length scales suggest a slight anisotropy of the flow

Correspondence to:

A. Brand,
Andreas.brand@eawag.ch

Citation:

Brand, A. and C. Noss (2017), High-resolution flow characterization close to the sediment-water interface in a run of the river reservoir, *Water Resour. Res.*, 53, 4286–4302, doi:10.1002/2016WR020203.

Received 29 NOV 2016

Accepted 5 MAY 2017

Accepted article online 12 MAY 2017

Published online 25 MAY 2017

High-resolution flow characterization close to the sediment-water interface in a run of the river reservoir

Andreas Brand^{1,2}  and Christian Noss³

¹Eawag, Swiss Federal Institute of Aquatic Science and Technology, Surface Waters - Research and Management, Kastanienbaum, Switzerland, ²Institute of Biogeochemistry and Pollutant Dynamics, ETH Zurich, Zurich, Switzerland,

³Institute for Environmental Sciences, University of Koblenz-Landau, Landau, Germany

Abstract A bistatic high-resolution acoustic profiler was used in order to characterize the lowermost boundary layer of a run of the river reservoir. The profiler allows determining the statistics of the three-dimensional flow field at a single point (sweet spot) as well as the measurement of the time averaged flow velocity profiles at 1 mm resolution around the sweet spot. Therefore, in addition to the flow statistics provided by single point acoustic Doppler profilers, mixing coefficients as well as production of turbulent kinetic energy can be calculated using a single device. Fitting of semiempirical relations to observed cospectra allowed eliminating artifacts as they result from coordinate system rotation during calculation of Reynolds stress profiles at millimeter resolution. While most parameters showed characteristics of a constant stress layer, length scales indicated anisotropy of the turbulent flow. Under these anisotropic near wall conditions, we found that the use of the commonly accepted Kolmogorov constants for the determination of dissipation rates using the inertial dissipation method is not valid any more. Instead, these constants vary with distance from the sediment water interface. We provide evidence that coefficients determined by numerical simulations are the appropriate choice also in field applications. In addition we resolved the viscous boundary layer close to the sediment-water interface in high resolution (1 mm) profiles and identified a double logarithmic layer above 1.5 cm at one location. The discrepancy of the scales as well as the double logarithmic layer suggests the existence of roughness elements upstream of the measurement sites.

1. Introduction

Flow in the close vicinity of the sediment-water interface (SWI) is an important abiotic factor shaping aquatic habitats. It governs the transfer of solutes to and from the sediment [Brand *et al.*, 2008; Bryant *et al.*, 2010], which in turn feeds back on microbial dynamics and reaction kinetics [Brand *et al.*, 2009; Frindte *et al.*, 2013]. Resuspension of particles, which can significantly enhance mineralization reactions and nutrient turnover in marine [Cloern, 1987; Tengberg *et al.*, 2003] as well as in limnetic systems [Kleeberg *et al.*, 2008], is also governed by the fluid flow close to the SWI [Brand *et al.*, 2015]. In lakes with a pronounced thermocline, bottom boundary layer turbulence generated by bottom shear can be the main source of vertical mixing [Goudsmit *et al.*, 1997] even though this mixing can be highly intermittent [Brand *et al.*, 2008]. In addition, benthic flow is an important driver for the adaptation and distribution of numerous benthic organisms [Vogel, 1994].

Until now, the in situ characterization of fluid flow in the zone close to the SWI in natural systems was difficult to achieve and only a few studies reported flow measurements in the last few centimeters to millimeters above the sediment-water interface in oceans using hot wire anemometers [Caldwell and Chriss, 1979; Chriss and Caldwell, 1984a,b] and gas tracer-based sensors in lakes [Brand *et al.*, 2007]. Especially the last millimeters above the SWI were not accessible for in situ measurements by commercially available systems. Until recently, acoustic velocimeters designed for field use had measurement volume sizes of only down to approximately 1 cm and were thus not suitable for measurements in the mm-range above the SWI [Dombroski and Crimaldi, 2007]. About 5 years ago, Nortek launched the Vectrino profiler which allows the recording of fluid flow at down to 1 mm resolution and at a frequency of up to 100 Hz. Similar to the single point acoustic Doppler velocimeters (ADV), the profiler consists of one central transmitter and four receivers (for a sketch of the system and the exact dimensions see Figure 1 in Brand *et al.* [2016]). Until now, most off-the-shelf acoustic velocity profilers (e.g., the acoustic doppler current profilers ADCP) consist of

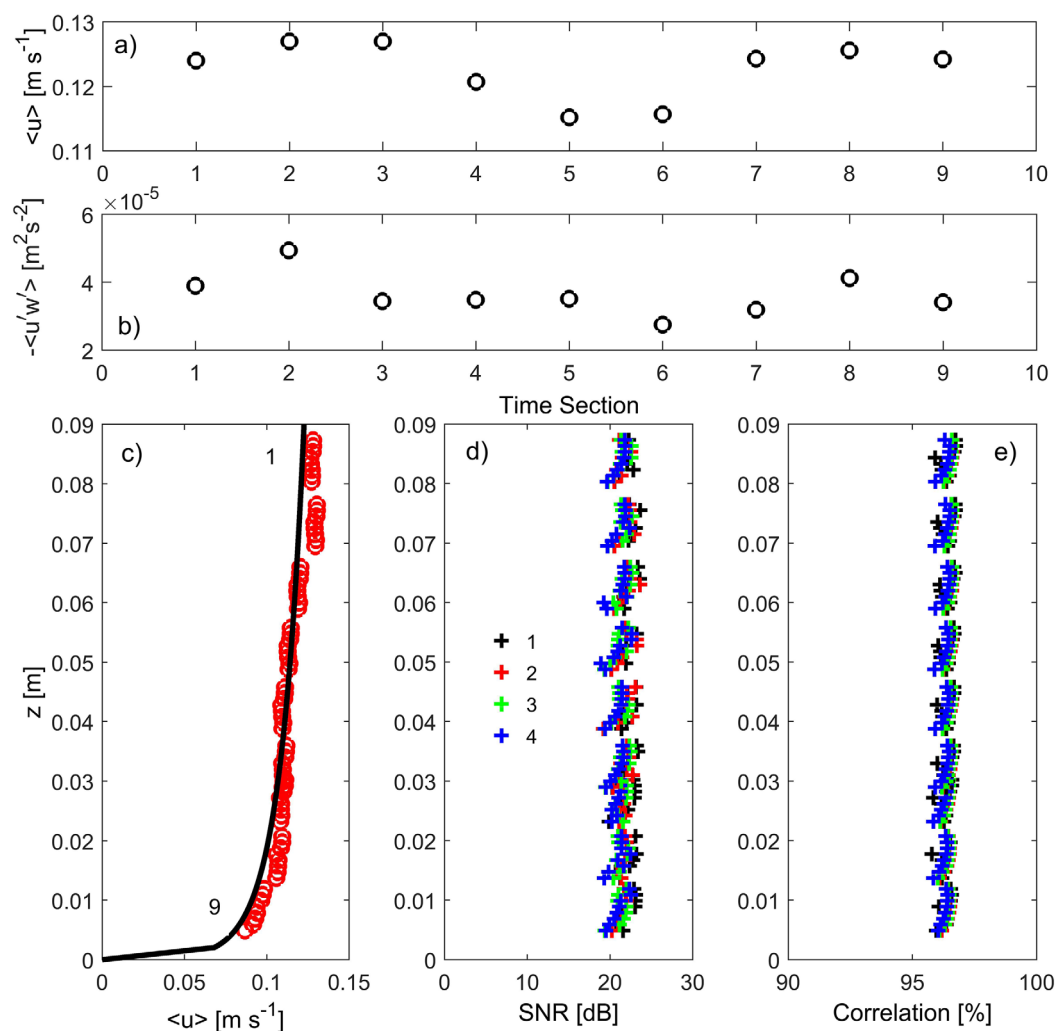


Figure 1. (a) Streamwise velocity and (b) Reynolds stresses recorded by the stationary ADV during the recording of consecutive 20 min time sections. (c) Composite profile recorded by the Vectrino Profiler (red circles) in comparison with the law of the wall fit (black line, equations (9) and (11)) using a u_* of $5.9 \times 10^{-3} \text{ ms}^{-1}$ and $a = 11.5$. “1” indicates the first recorded time section, “9” the last one. (d) Signal-to-noise ratios of individual beams and (e) their correlations.

several units which serve simultaneously as transmitters and receivers. These units, which are called monostatic systems, point in different directions and thus do not provide collocated three dimensional velocity measurements. This complicates especially the calculation of flow statistics [Stacey *et al.*, 1999]. The advantage of using separate transducers and receivers—so called bistatic systems—is the possibility to sample closely spaced, collocated volumes [Craig *et al.*, 2011], which allows an increase in spatial resolution. The fluid velocity is determined from the phase shift between consecutively emitted sound pulses which are reflected by the particles moving in the water. For details on the velocity calculations based on phase shift see e.g., Voulgaris and Trowbridge [1998] and Craig *et al.* [2011] and references therein. In contrast to standard ADVs which measure at a single point the Vectrino profiler records the backscattered signals at several consecutive time steps. This finally allows the measurement of a velocity profile [Craig *et al.*, 2011]. By default, the Vectrino profiler reports velocities along a 3.5 cm long profile ranging from 4 to 7.5 cm below the emitter. The profiler has already been used in situ to characterize the fluid flow at high resolution in tidal boundary layers [Pieterse *et al.*, 2015; Wengrove and Foster, 2014]. In a recent study, Brand *et al.* [2016] noticed that flow and turbulence statistics are most reliable in a rather narrow range which corresponds the point of maximum overlap sampled by the different receivers (this so-called sweet spot is located approximately 5 cm below emitter), while mean velocities are trustworthy over a 2 cm long vertical profile ranging from 4 to 6 cm below the emitter. Brand *et al.* [2016] also showed that Reynolds stresses are reliably

recorded over the two centimeter long profile as long as no coordinate system rotation is necessary. Still, most in situ measurements require such a rotation since an instrument tilt is hardly avoidable during deployment in natural systems. In the present study, we investigate the boundary layer flow of a run-of-the-river reservoir at several heights in the lowermost 10 cm above the SWI taking advantage of the profilers ability to provide a velocity profile simultaneously with flow statistics. In addition, we present high resolution measurements of time averaged flow velocities and Reynolds stresses in the lowermost 1.5 cm above the SWI. Based on these measurements we show that spectral fitting is a promising approach to correct for artifacts in the high resolution Reynolds stress profile induced by coordinate system rotation.

2. Unstratified Boundary Layer Flow

The main characteristic of turbulent bottom boundary layer flow is the turbulence production by shear due to the interaction between the moving fluid and the solid boundary [Schlichting and Gersten, 2000]. The bottom shear is frequently characterized by the shear velocity $u_* = \sqrt{\tau_b/\rho}$ where τ_b is the bottom shear stress and ρ is the fluid density. As we will show in the manuscript, the observed flow is well described by a uniform, two dimensional boundary layer flow with negligible stratification as it is frequently assumed in shallow systems like open channels and estuaries. Therefore we will only discuss the equations for this case in the following section. The theoretical curves of these various quantities for this boundary layer are shown by the solid lines in Figures 1 and 2. The turbulent Reynolds shear stress $-\langle u'w' \rangle$ is given by [e.g., Cardoso et al., 1989; Stacey and Ralston, 2005]

$$-\langle u'w' \rangle = u_*^2 \left(1 - \frac{z}{h}\right), \quad (1)$$

where z is the elevation above the SWI and h is the water depth. u' and w' denote the streamwise and vertical velocity fluctuations and $\langle \rangle$ the temporal arithmetic mean. In deep waters like lakes the term z/h becomes negligible and the region close to the SWI can be described as a constant shear layer where $-\langle u'w' \rangle = u_*^2$ [Wuest and Lorke, 2003]. In the constant stress region, Prandtl's mixing length hypothesis is expected to hold, which states that the mixing length of the turbulent eddies scales with the distance from the bed [e.g., Wuest and Lorke, 2003].

$$l_{BBL} = \kappa z, \quad (2)$$

where κ is the von Kármán constant which is typically around 0.41. In the turbulent region of the constant stress layer, the vertical gradient of streamwise velocity can be calculated as

$$\frac{\partial \langle u \rangle}{\partial z} = \frac{u_*}{\kappa z}. \quad (3)$$

For the well developed bottom boundary layer it is assumed that the production of turbulent kinetic energy

$$P = -\langle u'w' \rangle \frac{\partial \langle u \rangle}{\partial z} \quad (4)$$

balances the dissipation ε of kinetic energy and thus both quantities can be calculated by

$$\varepsilon = P = \frac{u_*^3}{\kappa z} \quad (5)$$

Since the Reynolds stress describes the vertical transfer of horizontal momentum in the constant stress layer

$$-\langle u'w' \rangle = u_*^2 = K_z \frac{\partial \langle u \rangle}{\partial z} \quad (6)$$

the eddy diffusivity K_z results from combining equations (3) and (6):

$$K_z = u_* \kappa z \quad (7)$$

Following Dillon [1982], the mixing length scale can be calculated by

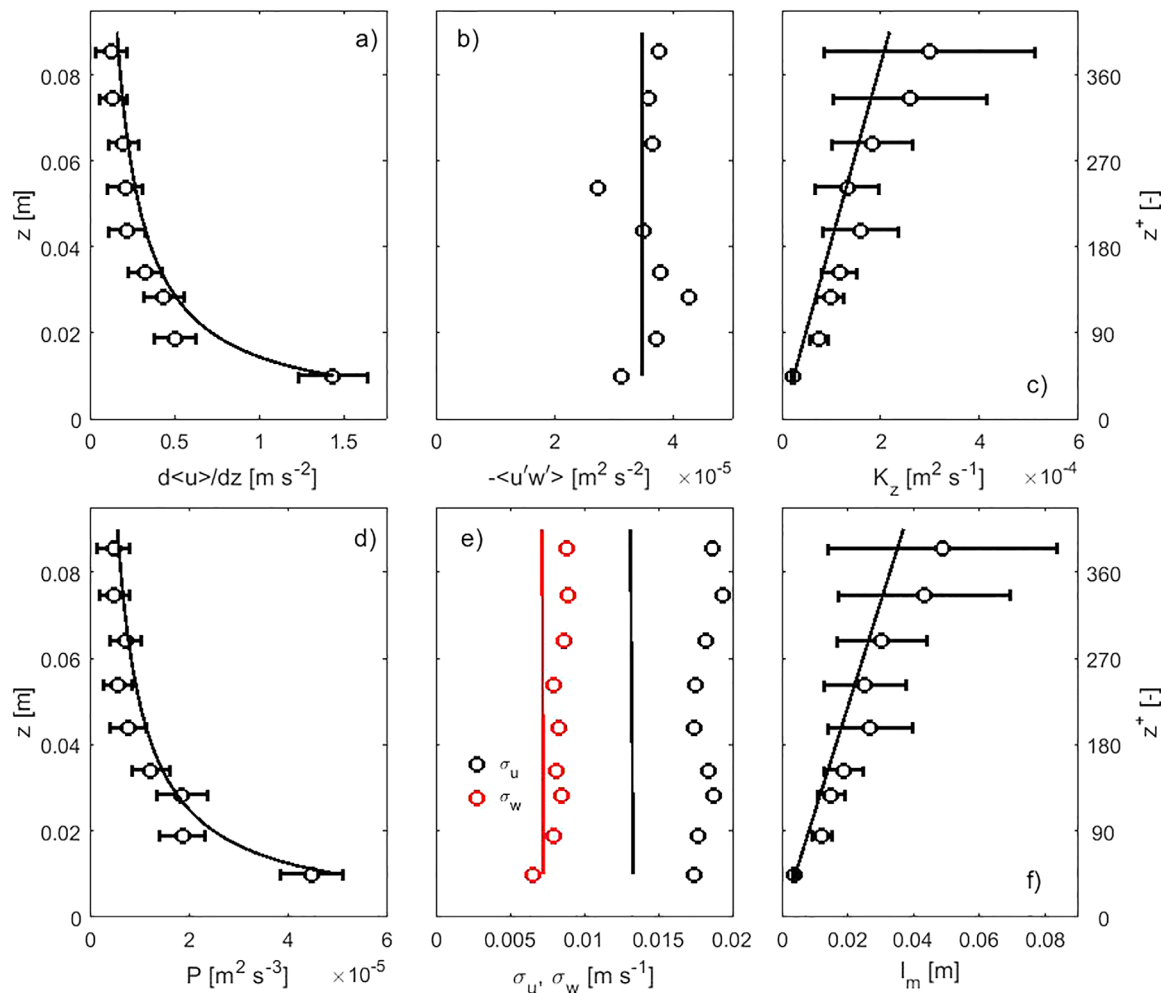


Figure 2. Measured turbulence parameters (circles) in comparison with the predictions of the bottom boundary layer theory (lines). Error bars were calculated using equations (A2) and (A3). (a) Vertical gradient of streamwise velocity, (b) Reynolds stress, (c) eddy viscosity, (d) production of turbulent kinetic energy. (e) standard deviations of streamwise and vertical velocities, (f) vertical mixing length scale.

$$l_m = \left(\frac{-\langle u'w' \rangle}{(d\langle u \rangle/dz)^2} \right)^{0.5} \quad (8)$$

which is expected to be close to l_{BBL} in the bottom boundary layer. Integration of equation (3) also results in the logarithmic streamwise flow velocity profile. Close to the SWI the turbulent fluctuations are damped by viscous forces and under hydraulically smooth flow conditions the logarithmic layer merges into the viscous sublayer. Under these conditions the logarithmic flow profile is described by [e.g., Chriss and Caldwell, 1984a]

$$\langle u(z) \rangle = \frac{u_*}{\kappa} \ln \left(\frac{z}{\delta} \right) + \frac{u_*^2}{\nu} \delta \quad (9)$$

for $z > \delta$. δ is the thickness of viscous sublayer and ν the kinematic viscosity. δ is given by

$$\delta = a \frac{\nu}{u_*}, \quad (10)$$

where a is an empirical constant, which is typically assumed to be around 11, but may vary significantly especially in environmental systems [Chriss and Caldwell, 1984a]. The velocity profile in the viscous sublayer is linear:

$$\langle u(z) \rangle = \frac{u_*^2}{\nu} z. \quad (11)$$

The turbulence cospectrum of the atmospheric as well as the oceanic boundary layer can be described by a semi-empirical function of wavenumber k , where $k=2\pi/\lambda$ and λ is the turbulent length scale [Kaimal et al., 1972; Soulsby, 1980]. The cospectrum for Reynolds stress can be described by [e.g., Gerbi et al., 2009]

$$\frac{Co_{u'w'}(k)}{\langle u'w' \rangle} = A \frac{1/k_0}{1 + (k/k_0)^{\frac{7}{3}}} \quad (12)$$

where k_0 is the roll-off wavenumber and A is a normalization constant to ensure that the integral of equation (12) is 1:

$$A = \frac{7}{3\pi} \sin\left(\frac{3\pi}{7}\right) \quad (13)$$

The spectrum described by equation (12) is approximately constant at wavenumbers smaller than k_0 and rolls off with $k^{-7/3}$ at wavenumbers larger than k_0 . k_0 is also the maximum of the variance preserving cospectrum [see Kirincich et al., 2010, Figure 4] which is defined as

$$k \frac{Co_{u'w'}(k)}{\langle u'w' \rangle} = Ak \frac{1/k_0}{1 + (k/k_0)^{\frac{7}{3}}}. \quad (14)$$

The roll-off wavenumber is related to the length scale λ_0 of the dominant flux-carrying eddies by $\lambda_0 = 2\pi/k_0$. Based on studies in the atmosphere this length scale was related to the distance from the bottom z as $\lambda_0/z = 8.3$ [Gerbi et al., 2009; Wyngaard and Cote, 1972] for unstratified flows. Therefore, k_0 can be estimated by

$$k_0 = \frac{2\pi}{8.3z}. \quad (15)$$

The wavenumber k is calculated by applying the frozen-field hypothesis [Taylor, 1938] as $k=2\pi f/U$ where f is the frequency and U the drift velocity, which is generally taken as the time-averaged free stream velocity [Gerbi et al., 2009].

The viscous dissipation rate ε can be determined from fitting the power spectral densities of the velocities. Under unstratified, isotropic turbulent conditions the inertial subrange of the power spectral density of the streamwise component (P_{uu}) is given by

$$\begin{aligned} P_{uu}(k) &= \alpha_u \varepsilon^{\frac{2}{3}} k^{-\frac{5}{3}} \\ P_{ww}(k) &= \alpha_w \varepsilon^{\frac{2}{3}} k^{-\frac{5}{3}} \end{aligned} \quad (16)$$

Under isotropic conditions α_u is $18/55 \times 1.56$ and $\alpha_w = 4/3\alpha_u$ [e.g., Monin and Yaglom, 1975].

Vertical profiles of standard deviations of streamwise and vertical velocities σ_u and σ_w for turbulent open channel flow were determined empirically to [Nezu and Rodi, 1986]:

$$\frac{\sigma_u}{u_*} = \frac{\langle u'^2 \rangle^{1/2}}{u_*} = D_u \exp\left(-\lambda_u \frac{z}{h}\right) \quad (17)$$

$$\frac{\sigma_w}{u_*} = \frac{\langle w'^2 \rangle^{1/2}}{u_*} = D_w \exp\left(-\lambda_w \frac{z}{h}\right) \quad (18)$$

where D_u , D_w , λ_u and λ_w are empirical constants with values of 2.26, 1.23, 0.88 and 0.67 respectively. The equations are valid in the region of $z^+ = zu_*/\nu > 50$ and $z/h < 0.6$.

3. Methods

3.1. Field Setup

Velocity profiles at 1 mm vertical resolution were recorded using a bistatic acoustic Doppler profiler (Nortek Vectrino profiler, Norway). For the dimensions and the capabilities of this instrument see Brand et al. [2016].

The profiler was mounted on a lander equipped with a step motor (KC Denmark). This allowed the positioning of the profiler at different elevations above the SWI. In addition, an acoustic Doppler velocimeter (ADV, Nortek Vector, Norway) was installed at 10 cm distance above the SWI. The SWI was determined using the internal bottom detection of the Vectrino probe which has an accuracy of 0.5 mm [Koca *et al.*, 2017]. Both instruments recorded data simultaneously at a sampling frequency of 32 Hz and time series of 20 minutes were recorded at each position of the Vectrino profiler. Care was taken to deploy the lander in such a way that the u -component of the flow velocimeters was aligned as well as possible with the streamwise current direction in order to ensure that the flow field was not disturbed by the lander. In order to align the velocities provided by the Vectrino profiler with the streamwise flow we performed a coordinate system rotation (see section 3.2 for details). For all deployments the rotation angles of the horizontal plane revealed a misalignment between the Vectrino beam system and the streamwise flow below 16° . Hence the flow was not disturbed by the frame of the lander.

Two field campaigns were conducted in Lake Wohlen, a run of the river hydropower reservoir known for its high methane emissions [DelSontro *et al.*, 2010]. The substrate of the sediment consists mainly of fine silt and clay with an organic matter content of about 2% [DelSontro *et al.*, 2010]. Measurements were performed at locations with water depths h between 4 and 6 m in the shallower part of the lake in approximately 50 m distance from the shoreline. The first campaign was conducted on the 11 June 2014, which was focusing on measurements with the profiler in the last centimeters above the SWI at two different locations with different flow velocities. At the first location with a water depth of 4 m, the flow velocity at 10 cm elevation above the SWI was 18.3 cm s^{-1} , while at the second location with a water depth of 6 m but identical elevation, the flow velocity was 31.1 cm s^{-1} . The second campaign was conducted on the 20 October 2015. During the second campaign, 9 high resolution profiles at various elevations between 1.0 and 8.5 cm above the SWI were recorded at one location over the duration of 4 h (Figure 1). The average flow velocity at this location was 12 cm s^{-1} at 10 cm elevation and the water level was 4.7 m.

3.2. Data Processing

Since a tilt and a slight misalignment during deployment is unavoidable, each 20 min section of the flow velocity data was rotated to ensure $\langle v \rangle = \langle w \rangle = 0$ and $\langle u \rangle$ corresponds to the streamwise velocity [Lee *et al.*, 2004]. The streamwise velocity profiles very close to the SWI were fitted to the composite profile described by equations (9) and (11) following Brand *et al.* [2016]. For the data obtained during the second campaign, flow statistics and spectra were always calculated at the sweet spot, which corresponds to the intersection of the transmitted and received beams of the profiler and provides velocities with the lowest noise levels [Brand *et al.*, 2016]. Vertical gradients of streamwise velocity were determined by linear regression of the time-averaged streamwise velocities determined by the profiler in $\pm 5 \text{ mm}$ distance from the sweet spot as a function of elevation.

Power spectral densities and cospectra were calculated using Welch's method [Welch, 1967] as implemented in Matlab. The spectra were averaged from 9 individual spectra calculated from data sections with a window size of 8192 data points with an overlap of 50% resulting in a frequency range between 0 and 16 Hz with a frequency step size of $\Delta f = 1.95 \times 10^{-3} \text{ Hz}$. Wave numbers were calculated from frequencies as $k = \langle u \rangle f$ where $\langle u \rangle$ was measured by the ADV. For spectral fitting, the observed variance preserving and integrated cospectra were subdivided into 70 frequency bins over the wavenumber range. All values in these bins were averaged in order to ensure equidistant data points when the spectra were plotted against $\log(k)$ (for more details, see Brand *et al.* [2008] and Kaimal and Gaynor [1983]). The effect of this procedure is illustrated in Figures 3a and 3b for the power spectral densities. The gray line shows the raw spectra with a constant frequency—and consequently—wavenumber step size, while the black circles show the binned data with constant step sizes in $\log(k)$. In the following we will refer to these averaged spectra as binned spectra.

In order to determine ε , we analyzed equations (16) and (17) following the method described by Bryant *et al.* [2010] which makes use of the fact that the inertial subrange can be identified as a horizontal line when P_{uu} and P_{ww} are multiplied by $k^{5/3}$ and plotted against k (Figures 3c and 3d). The inertial subrange can be identified as the horizontal section in the resulting spectrum (thin lines in Figures 3c and 3d). The average values of this horizontal part ($P_{uu}^{\text{inert}} k^{5/3}$ and $P_{ww}^{\text{inert}} k^{5/3}$), which are indicated by the solid black line in Figures 3c and 3d respectively, are used to calculate the dissipation rates as

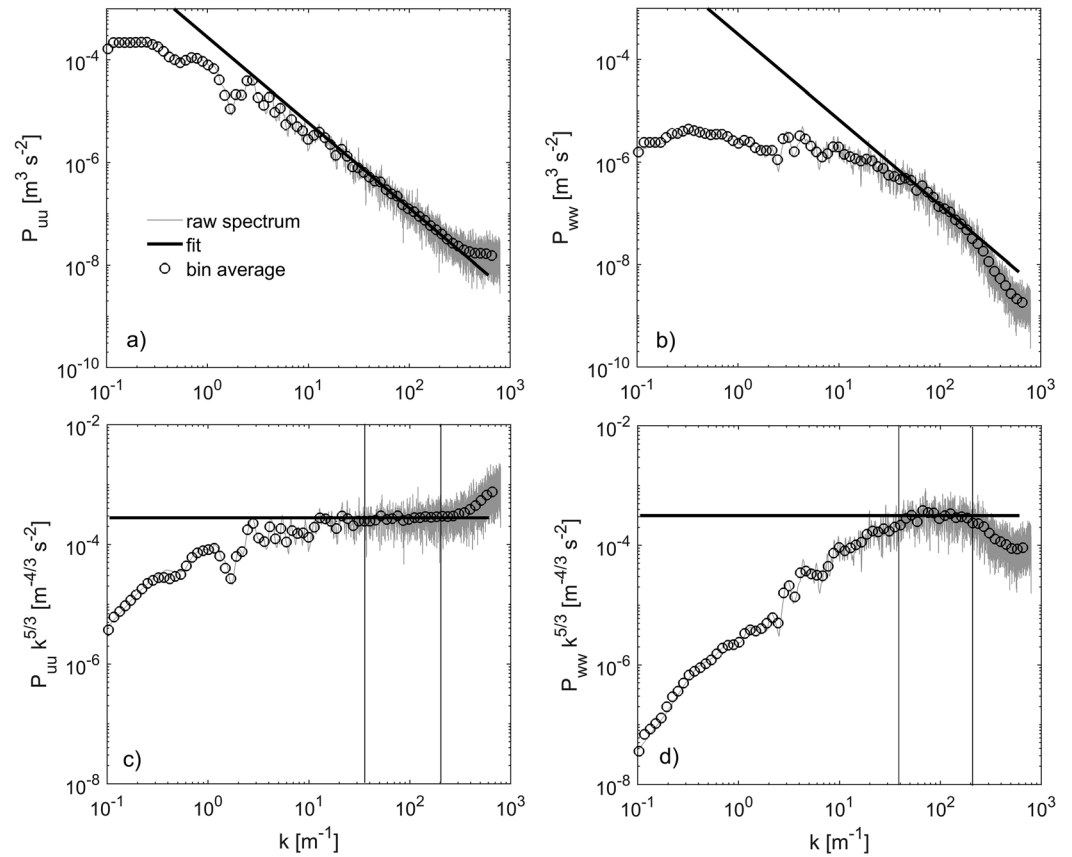


Figure 3. Power spectral densities recorded at 8.4 cm elevation of (a) streamwise and (b) vertical velocity. (c, d) Corresponding spectra multiplied by $k^{5/3}$ in order to identify the inertial subrange as the horizontal part of the spectrum. The solid black line shows the fit to the inertial subrange, the light gray line the raw data of the spectra and the circles the bin-averaged spectra according to equation (19). Thin vertical lines in (c) and (d) indicate the inertial subrange. Wavenumbers are reported in the unit radians per meter (m^{-1}).

$$\varepsilon_u = \left(\frac{p_{uu}^{\text{inert}} k^{5/3}}{\alpha_u} \right)^{3/2} \quad \text{and} \quad \varepsilon_w = \left(\frac{p_{ww}^{\text{inert}} k^{5/3}}{\alpha_w} \right)^{3/2} \quad (19)$$

where ε_u and ε_w denote the dissipation rates estimated from the streamwise velocity spectra and the vertical velocity spectra respectively. k_0 and $\langle u'w' \rangle$ were determined by simultaneous least squares fitting of the integral of equation (12) and the variance preserving spectrum (equation (14)) to the binned measured spectra following Gerbi *et al.* [2009]. In order to avoid an erroneous estimation of $\langle u'w' \rangle$ due to the contamination of the spectra by high frequency noise (for more details on noise contamination in the Vectrino profiler, see Brand *et al.* [2016]) only the 50 bins with the lowest wave numbers were considered for the fit. Uncertainties and errors of the flow parameters were calculated as described in Appendix A.

Integral length scales are defined as the spatial integral of the auto- and, accordingly, the cross-correlation function of velocity components [Stacey *et al.*, 1999; Tennekes and Lumley, 1972]. Applying Taylor's hypothesis of frozen turbulence these scales can be defined as [Stacey *et al.*, 1999]:

$$\begin{aligned} \lambda_{uw} &= U \int_0^\infty R_{uw}(\tau) d\tau \\ \lambda_u &= U \int_0^\infty R_{uu}(\tau) d\tau \\ \lambda_w &= U \int_0^\infty R_{ww}(\tau) d\tau \end{aligned} \quad (20)$$

where τ is the lag time and $R_{u_i u_j}(\tau)$ is the cross- or autocorrelation function

$$R_{u_i u_j}(\tau) = \frac{\langle u_i'(t) u_j'(t+\tau) \rangle}{\langle u_i'(t) u_j'(t) \rangle}. \quad (21)$$

u_i and u_j stand for the different velocity components as they are used in equation (20). For the calculations of the function for each time series recorded, autocorrelation functions were calculated every 612 data points using windows with a length of 5120 data points. The resulting 30 functions were subsequently averaged. Since smaller window sizes resulted in smaller length scales, window sizes were increased until the all length scales were constant. Increasing the 5120 data point window size by 20% resulted in an average change of the length scales by 2.5% which is negligibly small.

4. Boundary Layer Characterization by Stepwise Profiling

4.1. Mean Velocity Profile

In order to characterize the lowermost 9 cm above the SWI, we recorded 9 velocity profiles at different elevations during the second field campaign (Figure 1). We only considered profile sections with a time-averaged signal to noise ratio above 20 (Figure 1d) in order to ensure reliable velocity measurements [Brand *et al.*, 2016]. The time averaged correlation between acoustic pings was above 95% for these data (Figure 1e). During this field campaign, the streamwise velocity $\langle u \rangle$ measured by the ADV at 10 cm elevation varied between 11.5 and 12.7 cm s⁻¹ with an average value of 12.1 cm s⁻¹ (Figure 1a). The Reynolds stresses at this spot ranged between 2.8×10^{-5} m² s⁻² and 5.2×10^{-5} m² s⁻² with an average of 3.8×10^{-5} m² s⁻², which corresponds to $u_* = 0.62$ cm s⁻¹ (Figure 1b). The temporal variability of the flow is also reflected in the velocity profile, which was combined from the time sections sequentially recorded by the Vectrino profiler (Figure 1c). The least squares fit of the observed profile resulted in $u_* = 0.59$ cm s⁻¹, which is in good agreement with the averaged u_* , and $a = 11.5$ describes the observed profile well (Figure 1c).

4.2. Mixing Coefficients, Energy Production and Velocity Fluctuations

The ability of the profiler to provide reliable turbulence statistics at the sweet spot together with a profile of average flow velocities allows us to characterize the boundary layer flow with respect to mixing and energy budget (Figure 2). All parameters shown are compared with their theoretically expected values for a constant shear layer (equations (1–8), (17), and (18)). The recorded boundary layer generally shows the typical properties of a constant stress layer. The observed Reynolds stresses range between 2.8×10^{-5} m² s⁻² and 4.9×10^{-5} m² s⁻² (Figure 2b) and thus show a similar variability as the stresses recorded at a fixed position by the ADV (Figure 1b). This suggests that the variations are not caused by spatial variability but due to a slight temporal variability. $d\langle u \rangle/dz$, K_z , P and σ_w agree in the range of their uncertainty well with the theoretically expected values (Figure 2), while σ_u is on average 0.4 times larger than the values suggested by Nezu and Rodi [1986] for developed open channel flow (equations (17) and (18)). The ratio σ_w/σ_u is commonly assumed to be constant with a value of 0.55 [Nezu and Nakagawa, 1993] for turbulent channel flow, while we obtained a value of 0.44. Similar to our findings, Nikora and Goring [2000] observed values below 0.55 for $z/h < 0.1$. Close to the SWI ($z/h < 0.01$), values as low as 0.3 were observed in their study. Still, these very low values were attributed to weakly mobile beds, while values over fixed beds were around 0.4. Our measurements were conducted at shear velocities of up to 0.65 cm s⁻¹, which is 5–10 times lower than the ones reported by Nikora and Goring [2000]. Still, typical critical shear velocities of cohesive muddy sediments range between 0.5 and 1 cm s⁻¹ [Brand *et al.*, 2015; Sanford and Halka, 1993] and are therefore close to the shear velocity observed in our study. On the other hand, we did not observe the expected reduction in the von Kármán constant due to bed motion reported by Nikora and Goring [2000] which suggests that there is no occurrence of a moving bed in our study. While we can most likely rule out bed motion, our measurements for $z/h < 0.025$ were consistent with the observations of Nikora and Goring [2000] for immobile beds and result in similar σ_w/σ_u values. Direct numerical simulations performed by Kim *et al.* [1987] resulted in a σ_w/σ_u ratio of 0.76 at $z^+ = zu_*/\nu = 98$ which is higher than the experimentally determined values mentioned before. In addition, they showed an increase of σ_u by 25% from $z^+ = 98$ to $z^+ = 50$, while σ_w increases by 7%. Still, we do not observe this change (Figure 2e).

4.3. Length Scales

The mixing length l_m calculated by equation (8) is also in good agreement with the theoretical value l_{BBL} , while there is a slight, but systematic deviation which is still in the range of uncertainty (Figure 2f). A

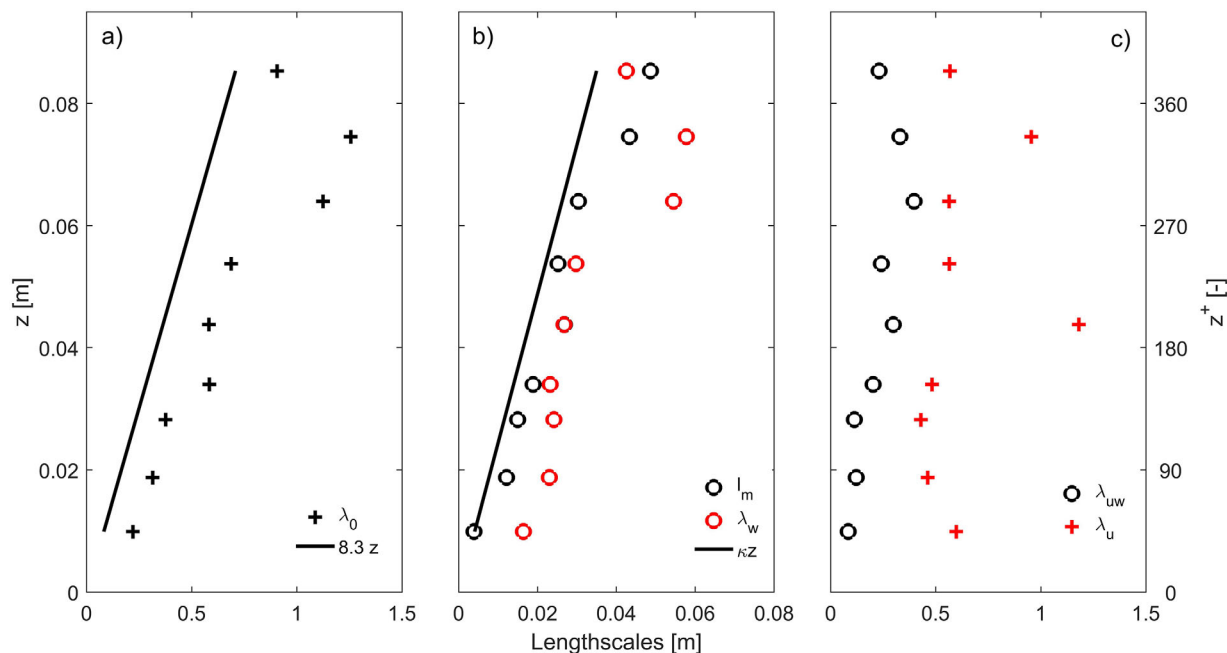


Figure 4. Comparison of the various length scales. (a) dominant eddy scale λ_0 determined by spectral fitting with the value given by Wyngaard and Cote [1972]; (b) vertical mixing length scale l_m , integral length scale of vertical velocity λ_w and theoretical prediction by boundary layer theory; (c) integral length scales for Reynolds stress λ_{uw} and streamwise velocity λ_u .

similarly systematic deviation by an average factor of 1.9 from the theory is observed when the dominant eddy length scale λ_0 obtained from spectral fitting is compared to the value reported by Wyngaard and Cote [1972] (Figure 4a). These deviations in combination with the overestimation of σ_u suggest that motions of scales larger than the ones determined by the bottom distance contribute to turbulent momentum transfer. In order to investigate the reasons for these deviations more closely, we analyzed the integral length scales (equations (20) and (21)). While there is a similar good agreement between l_{BBL} , l_m and λ_w (Figure 4b), λ_u is on average 22 times larger than λ_w , while λ_{uw} is about 5 times larger than λ_w and thus more similar to λ_w than λ_u (Figure 4c). These findings suggest anisotropy between streamwise and vertical length scales while the scale of vertical momentum transfer is confined by the other two scales. Such observations are usually explained by density stratification. However, profile recordings of temperature and conductivity during the measurements showed that there is no stratification by dissolved compounds and temperature in the last meter above the bottom. In addition, similar observations as ours have been reported for unstratified flow before. Stacey *et al.* [1999] reported anisotropic turbulence in an unstratified tidal flow in a 100 m wide channel. They also found that l_m was in good agreement with the theoretical predictions, while λ_{uw} were larger than λ_w and estimated that streamwise scales were 5–6 times larger than vertical ones which is similar to our observations.

4.4. Estimates of Energy Dissipation

If we calculate the dissipation estimates ε_u and ε_w using equation (19) and the constants for isotropic flow (in the following, we will refer to the use of these coefficients as the IDM method) the results differ on average by a factor of 1.6, while the discrepancy decreases with distance from the SWI (Figures 5a and 5b). This discrepancy is most likely due to the fact that the calculation of ε based on the IDM assumes isotropic turbulence, which might not be the case in our study. Under isotropic conditions α_w/α_u , which can be calculated from the Vectrino measurements as $p_{ww}^{inert}/p_{uu}^{inert}$ since ε itself is an isotropic quantity, has a constant value of 4/3 throughout the profile. In our case α_w/α_u increases from 0.62 at 1 cm distance from the SWI to 1.13 at 8.5 cm distance from the SWI (Figure 5c). This invalidates the assumptions of the IDM for our measurement. Jabbari *et al.* [2015] published a numerical study to evaluate the determination of ε using the inertial subrange of power spectra. They found that α values are not constant close to the SWI below $z^+ < 320$. Especially α_w shows a strong decrease below $z^+ = 150$, while a decrease of α_u was observed only at the very close distance to the SWI ($z^+ < 20$).

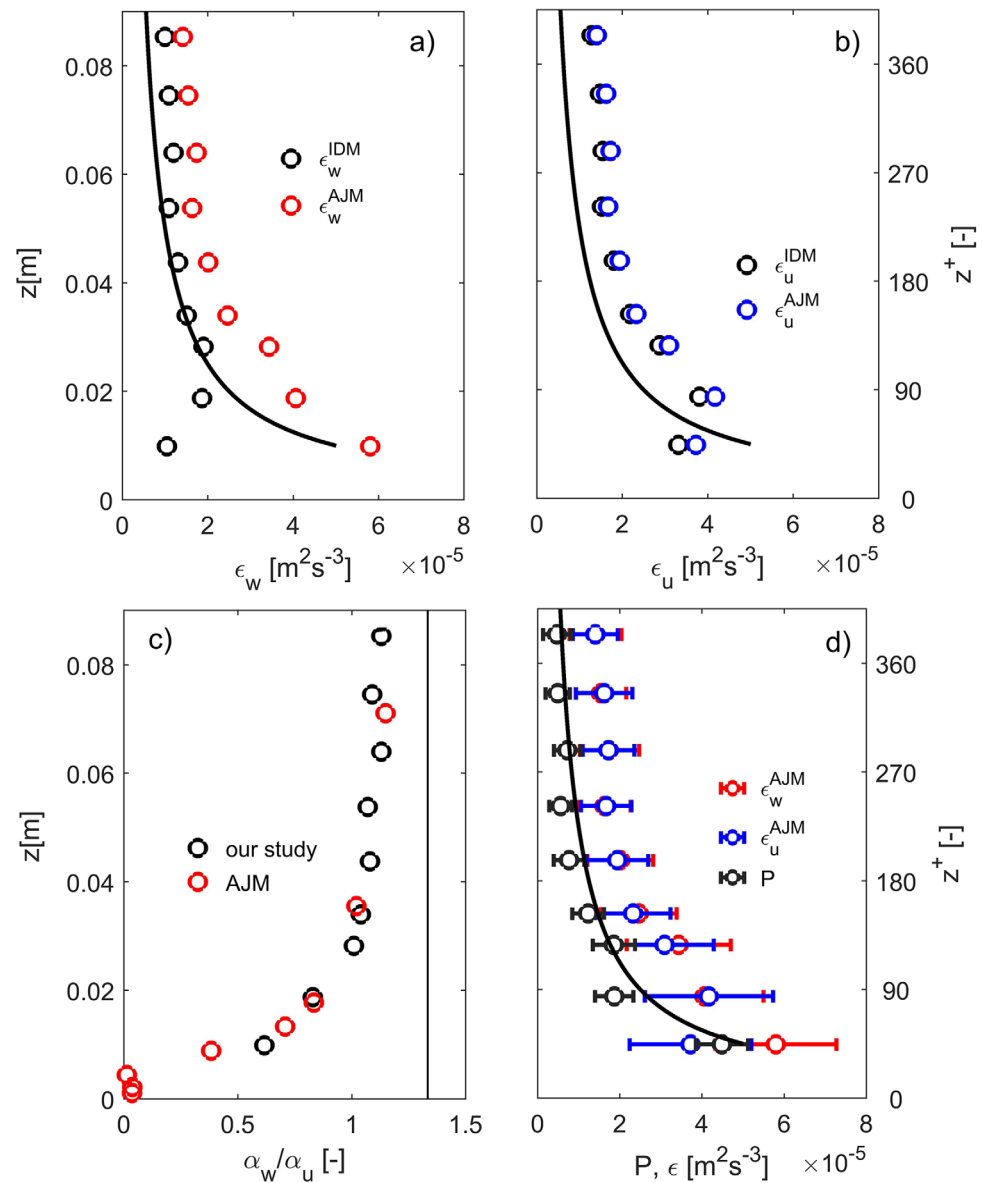


Figure 5. Analysis of the inertial dissipation method based on the Kolmogorov constants for anisotropic flow (IDM) in comparison with the numerical simulation study of *Jabbari et al.* [2015] (AJM). (a) Dissipation calculated using vertical velocity spectra and the constants of IDM and AJM. (b) Dissipation calculated using streamwise velocity spectra and the constants of IDM and AJM. (c) Ratio between vertical and along-stream Kolmogorov constants determined in our study in comparison with the values of *Jabbari et al.* [2015]. The vertical solid line denotes the value of 4/3 as generally used in the IDM. (d) Dissipation calculated based on AJM in comparison with production of turbulent kinetic energy. Solid lines in Figures 5a, 5b, and 5d denote the theoretical value based on bottom boundary layer theory.

The profile of α_w/α_u calculated using the Kolmogorov constants determined by *Jabbari et al.* [2015] are in excellent agreement with our measurements (Figure 5c). This suggests that the Kolmogorov constants provided by their modeling study are more appropriate for our near SWI study (in the following we will refer to the use of the constants to estimate ε determined by *Jabbari et al.* [2015] as the AJM). While there is no large difference between ε_u calculated using IDM and AJM, estimates based on the vertical velocities ε_w differ increasingly with decreasing distance from the SWI. When the AJM is used, ε_u and ε_w are in excellent agreement at $z^+ > 80$, while values differ at the lowermost measurement but they are still in the range of their uncertainty. One possible reason why we see a decrease in ε_u , which becomes smaller than P at the lowermost data point might be the fact that we reached the zone of net production of turbulent kinetic energy. Direct numerical simulations of boundary layer flow performed by *Kim et al.* [1987] show that P exceeds ε in the vicinity of the SWI [*Pope*, 2000]. They observed this discrepancy at $z^+ < 50$ with a

Table 1. Model Performance Parameters for Spectral Fitting of the Integrated Equation (12) and Equation (14)^a

| Measurement | Spectra | R^2 | $RMSE_{Fit}$ | $RMSE_{Avg}$ | SS |
|----------------|---------------------|-------|----------------------|----------------------|------|
| Vectrino | variance preserving | 0.74 | 8.6×10^{-2} | 1.1×10^{-1} | 0.41 |
| | integrated | 0.99 | 5.6×10^{-2} | 3.1×10^{-1} | 0.97 |
| ADV | variance preserving | 0.76 | 8.9×10^{-2} | 1.3×10^{-1} | 0.53 |
| | integrated | 0.99 | 5.1×10^{-2} | 2.9×10^{-1} | 0.97 |
| Vectrino (SWI) | variance preserving | 0.77 | 8.1×10^{-2} | 1.2×10^{-1} | 0.59 |
| | integrated | 0.99 | 3.6×10^{-2} | 3.5×10^{-1} | 0.99 |

^a"Vectrino" denotes the stepwise profiling measurement, while "Vectrino (SWI)" corresponds to the high resolution measurements close to the SWI. "ADV" measurements were conducted during the stepwise profiling measurements.

maximum of $P=1.8\varepsilon$ at $z^+=11.8$, while we observed the discrepancy at $z^+=50$, which corresponds to the commonly given elevation of the transition zone [Nezu and Nakagawa, 1993]. While the decrease of ε_u suggests this change, ε_w still increases. Though, estimates of ε_u are supposedly more robust in such a close vicinity to the SWI, since α_u used in the AJM is relatively constant at $z^+>40$, while α_w changes significantly in this zone [see Table 1 in Jabbari et al., 2015].

4.5. Cospectra of Vertical and Streamwise Velocities

Figure 6 and Table 1 show that the observed spectra of Reynolds stresses are described reasonably well by equations (12–14). Especially the R values close to 1 and the skill scores above 0.97 for the reproduction of the integrated spectra (Figures 6b and 6d; Table 1) indicate the high quality of the fits. The model performance parameters of the variance preserving spectra are lower with $R^2>0.75$ and $SS>0.41$ (Figures 6a and 6c; Table 1). This may be mainly explained by the fact that the measured variance preserving spectra contain a higher scatter than the integrated spectra. While the energy preserving spectra are in good agreement for $k/k_0>2$, the observed spectra are slightly below the theoretically expected spectrum at $0.2<k/k_0<2$. The scaled spectra are similar for the profiler and the ADV measurements (Figures 6a and 6c) confirming the validity of the profiler measurements. The negative values observed in the cospectra calculated from the ADV data above $k/k_0=10$ (Figure 6c) are most likely an artifact due to the introduction of

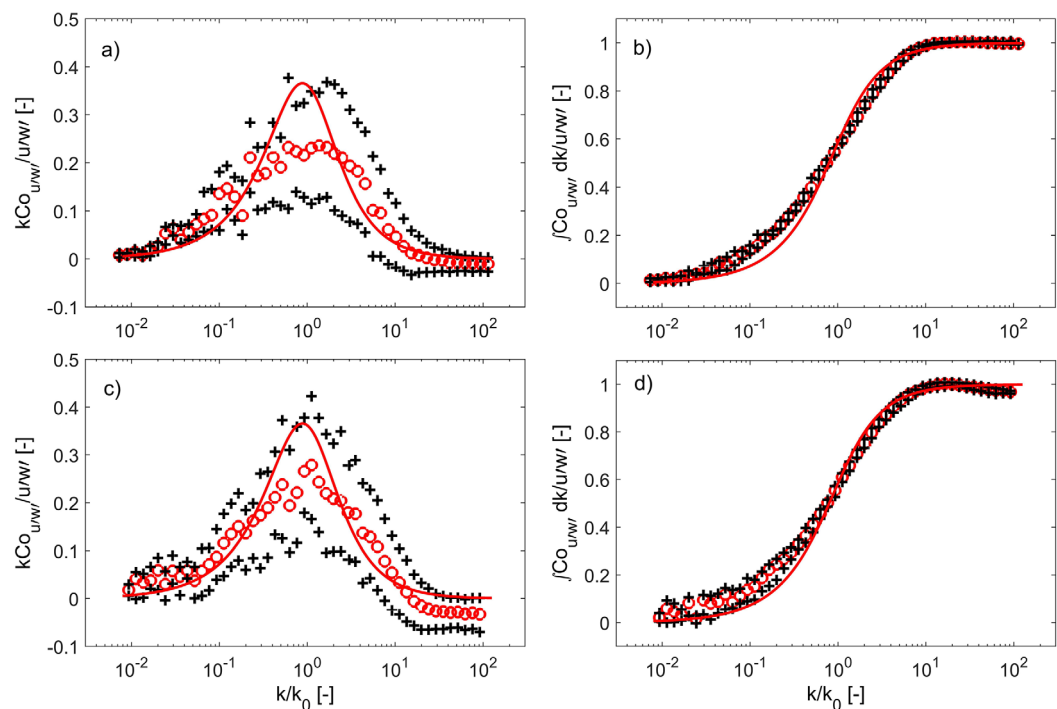


Figure 6. Normalized variance preserving (a, c) and integrated cospectra (b, d) of all time sections recorded shown in Figures 1 and 2. Red circles denote the median, and crosses the 25th and 75th percentile. Red lines show the theoretical spectra. (a, b) Spectra obtained from Vectrino data measured at the sweet spot at different elevations shown in Figures 2c and 2d: Spectra obtained from corresponding time sections recorded by the ADV recorded in 10 cm elevation (see Figure 1).

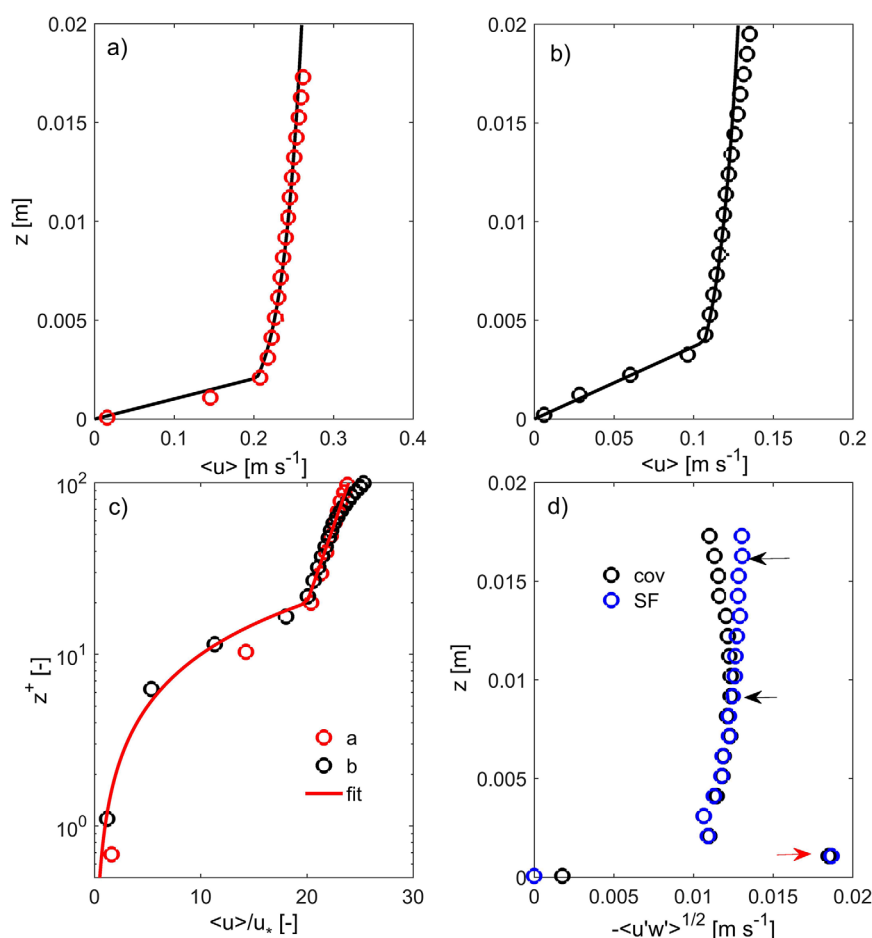


Figure 7. High-resolution profiles measured at the sediment-water interface. (a, b) Time averaged streamwise flow velocities observed during the first field campaign in comparison with the profiles obtained using equations (9) and (11). (c) Semi-logarithmic plot of the dimensionless streamwise velocity as a function of the dimensionless distance from the sediment for the profiles shown in Figures 7a and 7b in comparison with the theoretical profile (equations (9) and (11)). (d) Square-root of the Reynolds-stress corresponding to the measurement shown in subplot a. “cov” indicates that $-\langle u'w' \rangle$ was calculated as the covariance, “SF” denotes that $-\langle u'w' \rangle$ was calculated using spectral fitting. The black arrows indicate bins 3 and 11 whose spectral analysis is shown in Figure 8, the right arrow indicates an outlier most probably due to bottom interference.

correlated Doppler noise by coordinate system rotation. *Brand et al.* [2016] observed that noise in the Vectrino profiler mainly occurs in the high frequency range. While noise levels in $-\langle u'w' \rangle$ before coordinate system rotation are fairly low, noise in the variances of horizontal velocities $\langle u'^2 \rangle$ and $\langle v'^2 \rangle$ are much higher. A coordinate system rotation is necessary for most field measurements and causes a transfer of the noise of the horizontal variances into $-\langle u'w' \rangle$. Depending on the direction of the rotation this noise may lead to an over- or underestimation of $-\langle u'w' \rangle$ as it is in our case (Figure 6d). As *Brand et al.* [2016] have shown and we will illustrate in the next section, this effect becomes increasingly important with distance of the measurement cell from the sweet spot (Figures 7d and 8c). It is interesting to note that this effect is much less pronounced for the Vectrino profiler when data are determined at the sweet spot in a cell with a bin size of 1 mm (Figures 6a and 6b) compared to the ADV measurements which were conducted at a cell size of 14.9 mm (Figures 6c and 6d) suggesting that the noise contamination increases with increasing sampling volume size.

5. Measurements Next to the SWI

The measurements in the very close vicinity of the SWI were conducted at two different locations with different flow velocities. At the location shown in Figure 7a, $\langle u \rangle$ measured by the ADV in 10 cm elevation was 31.1 cm s⁻¹, and 18.3 cm s⁻¹ at the locations shown in Figure 7b. The flow profiles recorded at both sites

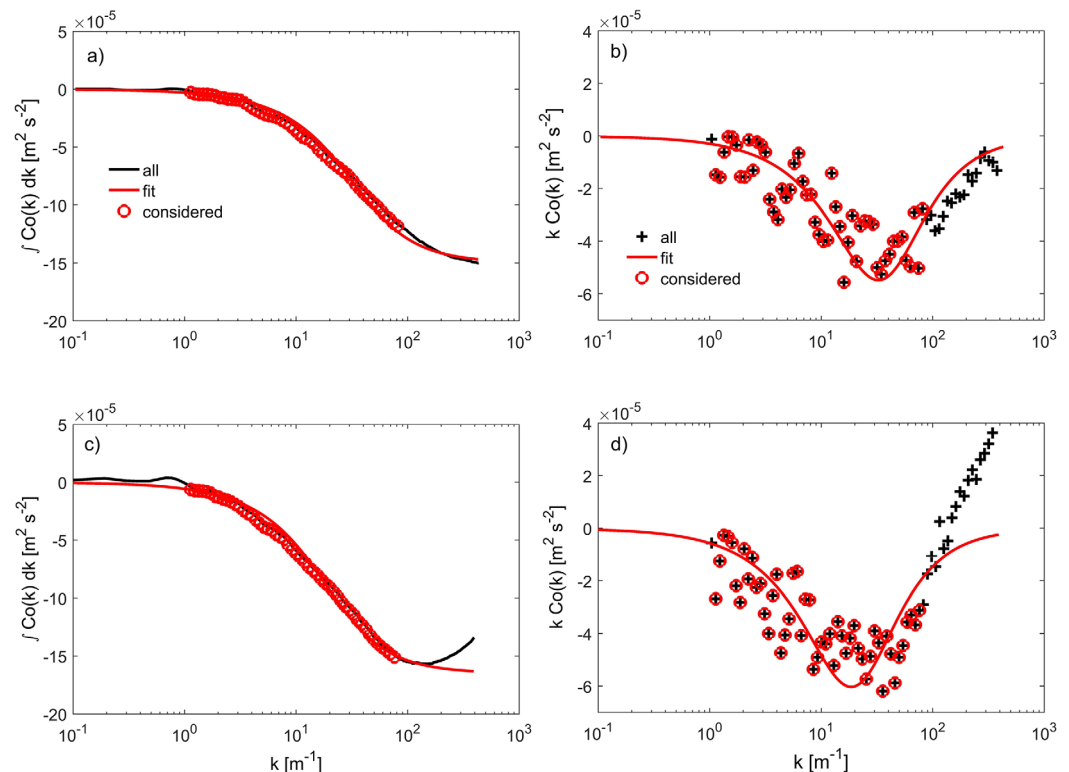


Figure 8. Cospectra for the Reynolds stresses shown in Figure (7)d. (a) Integrated cospectrum and (b) variance preserving cospectrum for bin 11 (sweet spot). (c) Integrated cospectrum and (d) variance preserving cospectrum for bin 3. The solid red line denotes the fit of the spectra. Black lines and crosses denote all data of the spectra, while only the data indicated by red circles were used for fitting.

show a pronounced viscous boundary layer with an adjacent logarithmic flow profile. Up to $z = 1.5$ cm both profiles can be well described by equations (9) and (11) using u^* values of 1.03 and 0.53 cm s^{-1} for the fast and slow flow respectively and an a value of 20 for both profiles. Both profiles collapse to a single one when nondimensionalized (Figure 7c). Even though the value of a is different from the frequently used value of 11.5, it is still well in the range reported by Chriss and Caldwell [1984a]. Both u^* values are slightly lower than those measured at 10 cm elevation by the ADV (1.35 and 0.9 cm s^{-1} for high and low flow respectively). The u^* determined for the fast flow by the ADV (1.35 cm s^{-1}) is almost identical with the value determined by the Vectrino profiler at $z = 1.7$ cm (1.30 cm s^{-1}). The streamwise flow profile at the low velocity site shows higher values than the theoretical predictions (Figures 7b and 7c). A possible explanation for this can be the existence of a double logarithmic layer as it has been described for larger scales e.g., by *Perlin et al.* [2005] and *Sanford and Lien* [1999]. This explanation is also supported by the difference in shear stress of 44% between the fitted value and the value determined in 10 cm elevation. Double logarithmic layers typically occur when the roughness elevations change e.g., by the existence of surface roughness elements upstream from the location of profile recording. As we will discuss in the next section, it is very likely that such a phenomenon occurred during our measurements.

When profiles of Reynolds stress are recorded over several bins with the Vectrino profiler at the fast velocity site, the signal can be contaminated with noise when the coordinate system is rotated (see *Brand et al.* [2016] and section 4.5 for more details). This especially applies to the bins in far distance of the sweet spot. The spectral fit method we applied in this manuscript following *Gerbi et al.* [2009] is a promising tool to solve this problem. Figures 8a and 8b show the cospectra (variance preserving and integrated) observed at bin 11, i.e., at the sweet spot (lower arrow in Figure 7d), which show negligible noise contamination, while the cospectra in bin 3 show noise contamination at wavenumbers above 100 m^{-1} (Figures 8c and 8d). A simultaneous spectral fit to the data which do not include the contaminated wavenumbers allows to compensate the underestimation of the Reynolds stresses (Figure 7d, 8c, and 8d) and might be the more promising approach than lowpass filtering, which can lead to an additional underestimation of the Reynolds stress [*Brand et al.*, 2016].

6. Potential Drivers of the Observed Near Bed Structure of the Bottom Boundary Layer

In our investigation we focused on the local boundary layer structure in the last 10 cm above the SWI. Right above the SWI we observed a viscous sublayer suggesting that the flow was hydraulically smooth or weakly transitional. In order to confirm the flow regime close to the SWI we calculated the roughness Reynolds number $Re^* = u_* k_s / \nu$. Shear velocities measured during our campaigns ranged from 0.53 cm s^{-1} to 1.03 cm s^{-1} . Even though we have no direct information on the bed roughness, we can estimate the equivalent bed roughness as $k_s = 3D_{90}$ following the average value determined by *VanRijn* [1982] for a plane bed. Since the sediments in Lake Wohlen mainly consist of clay and silt [*DeSontro et al.*, 2010], we used a D_{90} grain size of $62.5 \text{ }\mu\text{m}$, which corresponds to the upper limit of the grain size of silt and is therefore a conservative estimate. This results in a range of Re^* between 0.76 and 1.4, which is well below the critical threshold of 5 for the transition between hydraulically smooth and transitional flow [e.g., *VanRijn*, 1982]. Thus, the estimated roughness Reynolds number as well as the observed viscous sublayer indicate hydraulically smooth flow in the lowermost millimeters above the SWI. However, we observed deviations from the theoretically expected profile (equations (9) and (11)) at one of the locations during the first field campaign above 1 cm elevation (Figure 7b). In addition, the integral length scales and σ_u observed during the second field campaign also indicate anisotropic flow.

A possible reason for the occurrence of a double logarithmic layer and anisotropic flow might be the existence of single roughness elements like branches and stones upstream of the measurement sites. The existence of these elements is quite likely since the measurements were conducted relatively close to the shoreline where branches and reed might have fallen in the channel. While we did not have the means to observe such elements directly, discrepancies between P and ε can be indicative of such transitions [*Walter et al.*, 2011]. Indeed, ε_w as well as ε_u exceed P by average factors of 2.4 and 2.3 respectively (Figure 2d). Still, these differences are small compared to values reported by *Walter et al.* [2011] for a tidal system, which showed discrepancies of up to an order of magnitude downstream of eelgrass patches.

Our measurements suggest that different drivers influence the flow regime depending on the distance from the bottom. While hydraulically smooth flow indicated by the existence of a viscous boundary layer determines the flow regime at the very close vicinity of the SWI, sporadic roughness elements like branches, rocks and macrophytes located upstream from the measurement site might have influenced the fluid flow further above the SWI. With increasing distance from the SWI, the footprint of the region upstream of the measurement site which influences the measured signal increases [*Berg et al.*, 2007]. Therefore, the flow observed at various distances from the bottom may reflect the different influences the observed water parcels encountered.

While this study is a first step toward the characterization of boundary layer flow close to the SWI in natural systems, further studies are necessary to investigate the exact mechanisms which govern the flow of these layers. The Vectrino Profiler prove to be a useful tool to measure fluid flow parameters at high spatial resolution close to the SWI in the field and future studies should combine such profiler measurements with a thorough characterization of the bed properties upstream from and at the location of the flow profile recording e.g., by side scanning sonar or laser based topography measurements [*Roy et al.*, 2005].

7. Conclusions

In conclusion, the Vectrino profiler allowed the characterization of the lowermost region at the SWI in more detail than classical ADVs due to its ability to resolve turbulent quantities in combination with velocity profiles in the sub-cm scale. We were able to calculate mixing coefficients and production rates of TKE based on the data provided by one device at high spatial resolution. In general, the profiles were in reasonable agreement with the theoretically predicted values, while integrative length scales of streamwise velocity and vertical momentum transfer indicated anisotropy of the flow. This anisotropy is partly caused by the close vicinity of the SWI, while large-scale roughness elements upstream of the measurement site might have added to this effect as well. We found that the use of the inertial dissipation method using the generally accepted Kolmogorov constants for the determination of ε under these conditions is not valid any more. Our study provides evidence that the constants determined by numerical modeling [*Jabbari et al.*,

2015] are more appropriate in the close vicinity of the SWI in natural systems. In addition, we were able to observe the viscous boundary layer and to find indications of a double logarithmic layer in the very close vicinity of the SWI- an achievement which would not have been possible with standard ADVs with a spatial resolution of about 1.5 cm.

Appendix A: Uncertainty Estimation

The uncertainty of the vertical gradient of the streamwise velocity was calculated using the mean square error

$$MSE_{Fit} = \frac{1}{N} \sum_{n=1}^N (y_n - f(x_n))^2, \quad (A1)$$

where y_n is the measured value, N the total number of values and $f(x_n)$ is the value calculated by the function evaluated for the independent variable x_n . In the case of the velocity gradient y_n corresponds to the streamwise velocity, x_n to the elevation z and $f(x_n)$ to the function determined by linear regression. For linear regression, the uncertainty of the slope is then calculated by

$$\sigma_{\partial y / \partial x} = \left(\frac{MSE_{Fit}}{\frac{1}{N} \sum_{n=1}^N (x_n - \bar{x})^2} \right)^{1/2} \quad (A2)$$

where \bar{x} is the average of the independent variable [see e.g., Hartung, 1989]. In the present manuscript we calculate the uncertainty of the streamwise velocity gradient using this equation.

The uncertainties of each quantity calculated based on the vertical gradient of the streamwise velocity (P , see equation (4), K_z , see equation (6) and I_m , see equation (8)) were calculated based on the Gaussian law of error propagation [Hartung, 1989]

$$\sigma_Q = \sqrt{\sum_S \left(\frac{\partial Q}{\partial S} \right)^2 \sigma_S^2} \quad (A3)$$

where Q is the quantity under consideration and S the parameters used for the calculation of Q . In the case of most parameters we consider only one S which is the vertical gradient of the streamwise velocity for the uncertainty analysis. The uncertainty of $-\langle u'w' \rangle$ and its derived quantities is mainly due to temporal variation during the campaign (Figures 1a and 1b). Since this uncertainty is explicitly considered in our analyses and figures, we are not performing an additional formal error analysis for $-\langle u'w' \rangle$, u_* , and the standard deviations of streamwise and vertical velocity fluctuations σ_u and σ_w .

The error of the dissipation rates ε_u and ε_w were calculated based on the standard deviation of the quantities $\overline{p_{uu}^{inert} k^{5/3}}$ and $\overline{p_{ww}^{inert} k^{5/3}}$ determined from the power spectral densities multiplied by $k^{5/3}$ using equation (19). The standard deviations were calculated from the squared differences between the spectrum in the inertial subrange (gray line in Figures 3c and 3d) and the average value (solid black line in Figures 3c and 3d). The uncertainty in ε_{uu} and ε_{ww} was then calculated applying the Gaussian error propagation law (equation (A3)) to equation (19).

The quality of the spectral fits used to determine $-\langle u'w' \rangle$ and k_0 was investigated by several model performance parameters. The root mean square error of the model fit was calculated as $RMSE_{Fit} = MSE_{Fit}^{1/2}$. The skill score [Murphy and Epstein, 1989] was calculated as

$$SS = 1 - \frac{MSE_{Fit}}{MSE_{Avg}} \quad (A4)$$

where $MSE_{Avg} = \frac{1}{N} \sum_{n=1}^N (y_n - \bar{y})^2$ is the mean square error when the average value is used as the predictive function. A SS value larger than 0 indicates that the fitted model is a better predictor than a simple average. In addition we also calculated the Pearson correlation coefficient $R^2 = \text{cov}(y, f(x)) / (\sigma_y \sigma_{f(x)})$ where σ_y and

$\sigma_{f(x)}$ are the standard deviations of the measured and predicted variable respectively as well as the $RMSE_{Avg} = MSE_{Avg}^{1/2}$.

Acknowledgments

We thank Christian Dinkel and Matthias Zimmermann for the help in the field as well as Bernhard Wehrli und Johnny Wüest for fruitful discussions. The data used in this manuscript can be obtained on request by contacting either of the authors.

References

- Berg, P., H. Roy, and P. L. Wiberg (2007), Eddy correlation flux measurements: The sediment surface area that contributes to the flux, *Limnol. Oceanogr. Methods*, 52(4), 1672–1684.
- Brand, A., B. Muller, A. Wuest, C. Dinkel, N. P. Revsbech, L. P. Nielsen, O. Pedersen, L. R. Damgaard, L. H. Larsen, and B. Wehrli (2007), Micro-sensor for in situ flow measurements in benthic boundary layers at submillimeter resolution with extremely slow flow, *Limnol. Oceanogr. Methods*, 5, 185–191.
- Brand, A., D. F. McGinnis, B. Wehrli, and A. Wuest (2008), Intermittent oxygen flux from the interior into the bottom boundary of lakes as observed by eddy correlation, *Limnol. Oceanogr. Methods*, 53(5), 1997–2006.
- Brand, A., C. Dinkel, and B. Wehrli (2009), Influence of the diffusive boundary layer on solute dynamics in the sediments of a seiche-driven lake: A model study, *J. Geophys. Res.*, 114, G01010, doi:10.1029/2008JG000755.
- Brand, A., J. R. Lacy, S. Gladding, R. Holleman, and M. Stacey (2015), Model-based interpretation of sediment concentration and vertical flux measurements in a shallow estuarine environment, *Limnol. Oceanogr. Methods*, 60(2), 463–481.
- Brand, A., C. Noss, C. Dinkel, and M. Holzner (2016), High resolution measurements of turbulent flow close to the sediment-water interface using a bistatic acoustic profiler, *J. Atmos. Oceanic Technol.*, 33(4), 769–788.
- Bryant, L. D., C. Lorrai, D. F. McGinnis, A. Brand, A. Wuest, and J. C. Little (2010), Variable sediment oxygen uptake in response to dynamic forcing, *Limnol. Oceanogr. Methods*, 55(2), 950–964.
- Caldwell, D. R., and T. M. Chriss (1979), The viscous sublayer at the sea floor, *Science*, 205(4411), 1131–1132.
- Cardoso, A. H., W. H. Graf, and G. Gust (1989), Uniform flow in a smooth open channel, *J. Hydraul. Res.*, 27(5), 603–616.
- Chriss, T. M., and D. R. Caldwell (1984a), Universal similarity and the thickness of the viscous sublayer at the ocean-floor, *J. Geophys. Res.*, 89(C4), 6403–6414.
- Chriss, T. M., and D. R. Caldwell (1984b), Turbulence spectra from the viscous sublayer and buffer layer at the ocean floor, *J. Fluid Mech.*, 142, 39–55.
- Cloern, J. E. (1987), Turbidity as a control of phytoplankton biomass and productivity in estuaries, *Cont. Shelf Res.*, 7(11–12), 1367–1381.
- Craig, R. G. A., C. Loadman, B. Clement, P. J. Rusello, and E. Siegel (2011), Characterization and testing of a new bistatic profiling acoustic Doppler velocimeter: The Vectrino-II, in *2011 IEEE/OES/CWMT Tenth Working Conference on Current, Waves and Turbulence Measurement (Cwmt)*, edited by R. White, and A. J. Williams, pp. 246–252, IEEE, New York.
- DelSontro, T., D. F. McGinnis, S. Sobek, I. Ostrovsky, and B. Wehrli (2010), Extreme methane emissions from a swiss hydropower reservoir: Contribution from bubbling sediments, *Environ. Sci. Technol.*, 44(7), 2419–2425.
- Dillon, T. M. (1982), Vertical overturns—A comparison of Thorpe and Ozmidov length scales, *J. Geophys. Res.*, 87(C12), 9601–9613.
- Dombroski, D. E., and J. P. Crimaldi (2007), The accuracy of acoustic Doppler velocimetry measurements in turbulent boundary layer flows over a smooth bed, *Limnol. Oceanogr. Methods*, 5, 23–33.
- Frindte, K., W. Eckert, K. Attermeyer, and H.-P. Grossart (2013), Internal wave-induced redox shifts affect biogeochemistry and microbial activity in sediments: A simulation experiment, *Biogeochemistry*, 113(1–3), 423–434.
- Gerbi, G. P., J. H. Trowbridge, E. A. Terray, A. J. Plueddemann, and T. Kukulka (2009), Observations of turbulence in the ocean surface boundary layer: Energetics and transport, *J. Phys. Oceanogr.*, 39(5), 1077–1096.
- Goudsmit, G. H., F. Peeters, M. Gloor, and A. Wuest (1997), Boundary versus internal diapycnal mixing in stratified natural waters, *J. Geophys. Res.*, 102(C13), 27,903–27,914.
- Hartung, J. (1989), Statistik: Lehr- und Handbuch der angewandten Statistik, R. Oldenbourg Verlag, München.
- Jabbari, A., L. Boegman, and U. Piomelli (2015), Evaluation of the inertial dissipation method within boundary layers using numerical simulations, *Geophys. Res. Lett.*, 42, 1504–1511, doi:10.1002/2015GL063147.
- Kaimal, J. C., and J. E. Gaynor (1983), The Boulder atmospheric observatory, *J. Clim. Appl. Meteorol.*, 22(5), 863–880.
- Kaimal, J. C., Y. Izumi, J. C. Wyngaard, and R. Cote (1972), Spectral characteristics of surface-layer turbulence, *Q. J. R. Meteorol. Soc.*, 98(417), 563.
- Kim, J., P. Moin, and R. Moser (1987), Turbulence statistics in fully developed channel flow at low reynolds number, *J. Fluid Mech.*, 177, 133–166.
- Kirincich, A. R., S. J. Lentz, and G. P. Gerbi (2010), Calculating reynolds stresses from ADCP measurements in the presence of surface gravity waves using the cospectra-fit method, *J. Atmos. Oceanic Technol.*, 27(5), 889–907.
- Kleeberg, A., M. Hupfer, and G. Gust (2008), Quantification of phosphorus entrainment in a lowland river by in situ and laboratory resuspension experiments, *Aquat. Sci.*, 70(1), 87–99.
- Koca, K., C. Noss, C. Anlanger, A. Brand, and A. Lorke (2017), Performance of the Vectrino Profiler at the sediment–water interface, *J. Hydraul. Res.*, doi:10.1080/00221686.2016.1275049.
- Lee, X., W. Massman, and B. Law (2004), *Handbook of Micrometeorology—A Guide for Surface Flux Measurement and Analysis*, 250 pp., Kluwer Acad., Dordrecht, Netherlands.
- Monin, A. S., and A. M. Yaglom (1975), *Statistical Fluid Mechanics*, MIT Press, Cambridge, Mass.
- Murphy, A. H., and E. S. Epstein (1989), Skill scores and correlation coefficients in model verification, *Mon. Weather Rev.*, 117(3), 572–581.
- Nezu, I., and H. Nakagawa (1993), *Turbulence in Open-Channel Flows*, Taylor and Francis, Rotterdam, Netherlands.
- Nezu, I., and W. Rodi (1986), Open-channel flow measurements with a laser Doppler anemometer, *J. Hydraul. Eng.*, 112(5), 335–355.
- Nikora, V., and D. Goring (2000), Flow turbulence over fixed and weakly mobile gravel beds, *J. Hydraul. Eng.*, 126(9), 679–690.
- Perlin, A., J. N. Moum, J. M. Klymak, M. D. Levine, T. Boyd, and P. M. Kosro (2005), A modified law-of-the-wall applied to oceanic bottom boundary layers, *J. Geophys. Res.*, 110, C10S10, doi:10.1029/2004JC002310.
- Pieterse, A., J. A. Puleo, T. E. McKenna, and R. A. Aiken (2015), Near-bed shear stress, turbulence production and dissipation in a shallow and narrow tidal channel, *Earth Surf. Processes Landforms*, 40(15), 2059–2070.
- Pope, S. B. (2000), *Turbulent Flows*, Cambridge Univ. Press, New York.
- Roy, H., M. Huettel, and B. B. Jorgensen (2005), The influence of topography on the functional exchange surface of marine soft sediments, assessed from sediment topography measured in situ, *Limnol. Oceanogr. Methods*, 50(1), 106–112.
- Sanford, L. P., and J. P. Halka (1993), Assessing the paradigm of mutually exclusive erosion and deposition of mud, with examples from upper Chesapeake Bay, *Mar. Geol.*, 114(1–2), 37–57.

- Sanford, T. B., and R. C. Lien (1999), Turbulent properties in a homogeneous tidal bottom boundary layer, *J. Geophys. Res.*, *104*(C1), 1245–1257.
- Schlichting, H., and K. Gersten (2000), *Boundary Layer Theory*, 8th ed., Springer, Heidelberg.
- Soulsby, R. L. (1980), Selecting record length and digitization rate for near-bed turbulence measurements, *J. Phys. Oceanogr.*, *10*(2), 208–219.
- Stacey, M. T., and D. K. Ralston (2005), The scaling and structure of the estuarine bottom boundary layer, *J. Phys. Oceanogr.*, *35*(1), 55–71.
- Stacey, M. T., S. G. Monismith, and J. R. Burau (1999), Measurements of Reynolds stress profiles in unstratified tidal flow, *J. Geophys. Res.*, *104*(C5), 10,933–10,949.
- Taylor, G. I. (1938), The spectrum of turbulence, *Proc. R. Soc. London, Ser. A*, *164*(A919), 476–490.
- Tengberg, A., E. Almroth, and P. Hall (2003), Resuspension and its effects on organic carbon recycling and nutrient exchange in coastal sediments: In situ measurements using new experimental technology, *J. Exp. Mar. Biol. Ecol.*, *285*, 119–142.
- Tennekes, H., and J. L. Lumley (1972), *A First Course in Turbulence*, 300 pp., MIT Press, Cambridge, Mass.
- VanRijn, L. C. (1982), Equivalent roughness of alluvial bed, *J. Hydraul. Div. Am. Soc. Civ. Eng.*, *108*(10), 1215–1218.
- Vogel, S. (1994), *Life in Moving Fluids*, 469 pp., Princeton Univ. Press, Princeton, N. J.
- Voulgaris, G., and J. H. Trowbridge (1998), Evaluation of the acoustic Doppler velocimeter (ADV) for turbulence measurements, *J. Atmos. Oceanic Technol.*, *15*(1), 272–289.
- Walter, R. K., N. J. Nidzieko, and S. G. Monismith (2011), Similarity scaling of turbulence spectra and cospectra in a shallow tidal flow, *J. Geophys. Res.*, *116*, C10019, doi:10.1029/2011JC007144.
- Welch, P. D. (1967), Use of fast fourier transform for estimation of power spectra—A method based on time averaging over short modified periodograms, *IEEE Trans. Audio Electroacoust.*, *15*(2), 70–73.
- Wengrove, M. E., and D. L. Foster (2014), Field evidence of the viscous sublayer in a tidally forced developing boundary layer, *Geophys. Res. Lett.*, *41*, 5084–5090, doi:10.1002/2014GL060709.
- Wuest, A., and A. Lorke (2003), Small-scale hydrodynamics in lakes, *Annu. Rev. Fluid Mech.*, *35*, 373–412.
- Wyngaard, J. C., and O. R. Cote (1972), Cospectral similarity in the atmospheric surface layer, *Q. J. R. Meteorol. Soc.*, *98*(417), 590–603.